Editorial Manager(tm) for Journal of Electronic Materials
Manuscript Draft

Manuscript Number: JEMS-2111

Title: Intercalation: building natural superlattice for better thermoelectric performance in layered chalcogenides

Article Type: S.I.: ICT2010

Keywords: Natural superlattice; Thermoelectric; Misfit layer compounds; Thermal conductivity

Corresponding Author: Chunlei Wan,

Corresponding Author's Institution:

First Author: Chunlei Wan

Order of Authors: Chunlei Wan; Yifeng Wang; Ning Wang; Wataru Norimatsu; Michiko Kusunoki; Kunihito Koumoto

Intercalation: building natural superlattice for better thermoelectric performance in layered chalcogenides

Chunlei Wan[1,2], Yifeng Wang[1,2], Ning Wang[1], Wataru Norimatsu[2,3], Michiko Kusunoki[2,3] and Kunihito Koumoto [1,2,*]

[1] Graduate School of Engineering, Nagoya University, Nagoya, Japan

[2] CREST, Japan Science and Technology Agency, Tokyo, Japan

[3] EcoTopia Science Institute, Nagoya University, Nagoya, Japan

* Corresponding author's email: koumoto@apchem.nagoya-u.ac.jp

Abstract

A natural superlattice with a composition of $(SnS)_{1.2}(TiS_2)_2$ is built by intercalating an SnS layer into the van der Waals gap of layered TiS_2, as has been directly observed by HRTEM. In the direction parallel with the layers, the thermoelectric performance is found to be improved, as the electron mobility was maintained while the phonon transport is significantly suppressed, which was identified due to softening of the transverse sound velocites because of the weakened interlayer bonding. In the direction perpendicular to the layers, the lattice thermal conductivity of $(SnS)_{1.2}(TiS_2)_2$ is even lower than the predicted minimum thermal conductivity and phonon localization due to the translational disorder of the SnS layers in the direction parallel with the layers possibly accounts for it. We propose a large family of misfit layer compounds $(MX)_{1+x}(TX_2)_n$ (M = Pb, Bi, Sn, Sb, Rare earth elements; T = Ti, V, Cr, Nb, Ta, X = S, Se; n = 1, 2, 3) with a natural superlattice structure as possible candidates of high-performance thermoelectric materials.

Keywords: Natural superlattice, Thermoelectric, Misfit layer compounds, Thermal conductivity

1. Introduction

Thermoelectric materials are being intensively explored for various energy supply or conservation nowadays, which are considered as a promising solution for the impending energy crisis and global climate change. [1] The efficiency of a thermoelectric material can be described by the figure of merit $ZT = S^2\sigma/k$, where S, σ, and k represent Seebeck coefficient, electrical conductivity and thermal conductivity, respectively. Since the ZT values of the current thermoelectric materials are too low for cost-effective applications, various efforts have been made to improve them. Over the past decade, almost all the most significant progresses of thermoelectric materials have been made by the strategy of reducing lattice thermal conductivity, including rattling atoms [2,3], nanostructuring [4,5], low dimensionality [6,7], etc. Since there is an acknowledged concept [8] that thermal conductivities of solid materials cannot get below k_{min} (the thermal conductivity values of their amorphous state), an upper limit of ZT value seems to be in front if this strategy goes on. The dawn appears in the disordered layered WSe_2 film, in which the thermal conductivity reaches 0.05 W/mK, which is 6 times lower than the predicted k_{min} value. [9] Although the underlying mechanism is still not so clear, a successful example has appeared by applying layered superlattice structure into the thermoelectric materials design. In Venkatasubramamian's work [10], a superlattice film was fabricated by alternatively stacking Bi_2Te_3 and Sb_2Te_3, which attains a low thermal conductivity of 0.22 W/m.K. Meanwhile, the electron mobility was maintained because of the small band offset of the constituent materials Bi_2Te_3 and Sb_2Te_3. Finally, a high ZT value of 2.4 at 300 K was achieved. Even though, a shortage exists for the superlattice film, as the high-cost MQW (Multiple Quantum Wall) manufacturing processes can hardly allow fabricating thick films with large area that can afford large heat or current loads in ordinary use. [11] Moreover, a recent of study of PbTe/PbSe superlattice casts some doubt on the repeatability of low thermal conductivity for this artificial structure. [12]

In this paper, we propose a natural superlattice material by intercalating a layer of SnS into the van der Waals gap of layered TiS_2. The TiS_2 layer can provide thermopower as well as electron pathway according to Imai's research on TiS_2 single crystal. [13] The intercalated SnS layer can suppress the transport of phonons by the interaction between the SnS layer and TiS_2 layer and/or disruption of the periodicity of TiS_2 in the direction perpendicular to the layers. By using the conventional pressure sintering techniques (Hot pressing or spark plasma sintering), the layers of the polycrystalline grains became highly oriented due to anisotropic bonding of this natural superlattice structure, thereby enabling low-cost fabrication of large-scale polycrystalline product with its thermoelectric properties close to those of single crystals or artificial films. This natural superlattice also shows high thermodynamic stability and repeatability of thermoelectric properties.

Furthermore, the structure of these natural superlattice materials can be varied to some extent, including the species of the host material, the intercalated material as well as the ratio of these two components, thus constituting the large family of chalcogenide misfit layer compounds, $(MX)_{1+x}(TX_2)_n$ (M = Pb, Bi, Sn, Sb, Rare earth elements; T = Ti, V, Cr, Nb, Ta, X = S, Se; n = 1, 2, 3). [14] Therefore, this large family of misfit layer compounds are now introduced as new possible candidates for high-performance bulk thermoelectric materials. Some pioneering work of this type of compounds has been done, but they were still fabricated in the form of a film, the thickness of which can only be 50 to 100 nm by a designed synthesis method. [15,16] Also, ZT values were never reported, making this kind of material questionable to be a thermoelectric material.

2. Experimental

Both TiS_2 and $(SnS)_{1.2}(TiS_2)_2$ were prepared using the reported solid-liquid-vapor reaction method [17]. For both TiS_2, and $(SnS)_{1.2}(TiS_2)_2$, the constituent elements are weighted and mixed according to the stoichiometric ratio. The mixture powder was sealed in an evacuated

silica tube, which was then fired in an electrical furnace. The heating condition for TiS_2 is 600^{o}C for 6 days and the condition for $(SnS)_{1.2}(TiS_2)_2$ is 500^{o}C for 12 h, then at 800^{o}C for 48 h. The heating rate was fixed at 0.5^{o}C/h to avoid any explosive danger due to overpressure of sulfur. The obtained powders with luster were ground and sieved. The spark plasma sintering (SPS) method (SPS-1050, Sumitomo Mining Coal Mining Co. Ltd.) was used to densify the powders at 700^{o}C for 10 min under the pressure of 50 MPa into a pellet with diameter of 15 mm and thickness of 6 mm. Since the microstructure of the pellet is highly anisotropic, it was deliberately machined for thermoelectric properties measurements in the directions parallel and perpendicular to pressure.

The densities of the samples were measured using the Archimedes method. The phase composition was characterized by the X-ray diffraction measurements (RINT-2100, Rigaku). For HRTEM observation, a piece of sample was cut from the sintered pellet in the direction perpendicular to the pressure and polished to 100 microns. Both sides of this thin piece were then bonded with two 1-mm-thick standard silicon wafers using the G2 resin. One end of these stacked sheets was adhered to a copper ring for reinforcing and the other end is further mechanically polished and finally ion-thinned. The Seebeck coefficient and electrical conductivity were measured simultaneously by a conventional steady state method and a four-probe method, respectively, in an Ar atmosphere at 300–773K (RZ-2001K, Ozawa Science). The carrier concentration was determined by Hall effect measurement with a van der Pauw electrode configuration under vacuum of 10^{-3} Pa over the same temperature range (Resi Test 8300, Toyo Technica). The heat capacity and the thermal diffusivity were measured by differential scanning calorimetry (DSC-2910, TA Instruments) and laser-flash method (TC-9000V, ULVAC-RIKO), respectively. The thermal conductivity was calculated as a product of density, heat capacity and thermal diffusivity. The sound velocities including one longitudinal and two transverse modes were measured by the ultrasonic pulse-echo method (Model 5800 PR, Olympus).

3. Results

3.1. Microstructure

The stage-2 compound $(SnS)_{1.2}(TiS_2)_2$ consists of alternative stacking of one SnS layer and paired TiS_2 layers and its crystal structure can be analyzed by analogy with the available data of stage-1 compound $(SnS)_{1.2}TiS_2$, as the subsystem of SnS and TiS_2 are more or less identical in these two kinds of compositions. [18,19] (The crystal structure of $(SnS)_{1.2}TiS_2$ is proved in the supporting material). Both of the two subsystems, SnS and TiS_2, of $(SnS)_{1.2}(TiS_2)_2$ are triclinic. The space groups are C1- for SnS and F-1 for TiS_2. The SnS layer consists of deformed slices of SnS with a thickness of half the cell edge of the distorted NaCl-type SnS. Each Sn atom is coordinated by five S atoms within the same layer and two or three S atoms of the TiS_2 layers. The Sn atoms are slightly pushed out of the *a*-*b* plane with respect to the sulfur atoms in the same plane. The structure of the TiS_2 part is hardly distorted compared to the crystal structure of 1T-TiS_2, in which Ti is octahedrally coordinated. The Ti atoms have a trigonally antiprismatic coordination by six S atoms. In $(SnS)_{1.2}(TiS_2)_2$, the van der Waals gap still exists between the paired TiS_2 layers as in 1T-TiS_2. The SnS layer and the paired TiS_2 layers stack in the direction of *c* axis, although the two *c* axes of the two subsystems slightly diverge. Inside the layers, the b axes are parallel and of equal length while the *a* axes, being also parallel, have different lengths and the ratio is about 3:5. Therefore, the value of 1.2 in the chemical formula of $(SnS)_{1.2}(TiS_2)_2$ is obtained by taking account of the ratio of lattice parameters and number of atoms contained in one unit cell.

The crystal structure of $(SnS)_{1.2}(TiS_2)_2$ can hardly be refined by XRD pattern here, due to the presence of translational disorder, which will be shown below. The atomic structure along the incommensurate axis ([100] zone axis) is directly observed by HRTEM, as shown **Fig.** 1. The layered structure is shown, though detailed composition cannot be discerned immediately. We simulated patterns of separated SnS and TiS_2 layers using the the available structure data

of $(SnS)_{1.2}TiS_2$, which is in perfect agreement with the observed pattern. (See the square in white frame in **Fig.** 1). It then allows reconstruction of the whole crystal structure of $(SnS)_{1.2}(TiS_2)_2$ along the *a* axis by "translating" the observed pattern, which is shown in the right side of Fig. 1. It can be seen that the SnS layer and the paired TiS_2 layers stack alternatively as expected. The paired TiS_2 layers, separated by a van der Waals gap, almost stack in the same way as that in pure TiS_2. In contrast to the consistency of TiS_2 layers stacking in the whole crystal, the relative position between the SnS layer and TiS_2 layer vary. The SnS layers deposited on both sides of the same paired TiS_2 reference layers occupy two different relative positions. The Sn atoms of the SnS layer either reside in the middle of the two sulfur atom rows of the neighboring TiS_2 layer or stay exactly vertical to one of them by a translational displacement of *b*/4 along the *b* axis. In the direction of the commensurate *b* axis, the lattice parameters of SnS and TiS_2 are equal and the first case is reported in almost all the previous structural study of misfit layer compounds. [14,20-22] The second case has rarely been observed, and we anticipate that strain may play a role and the translational disorder occurs during pressure sintering.

The layered structure of $(SnS)_{1.2}(TiS_2)_2$ can be better observed in the [130] zone axis view in **Fig.** 2. It clearly shows that the paired TiS_2 layers and single SnS layer stack alternatively, making a total repeating unit cell length of 1.74 nm. The TiS_2 subsystem is not clear here because of superposition of the atoms in this direction. A computer simulation using the available structure data of the SnS subsystem in $(SnS)_{1.2}(TiS_2)_2$ shows perfect agreement with the HRTEM image. The arrangement of SnS layers in $(SnS)_{1.2}(TiS_2)_2$ is then reconstructed, as shown in **Fig.** 2. It can be found that the SnS layers are stacked with completely random transverse displacement normal to the *c* axis, which can be further evidenced by the presence of diffuse streak in the electron diffraction pattern. The lack of correlation between the successive SnS layers gives rise to planes of diffuse intensity instead of well-defined reflections. The completely random arrangement of the SnS layers in the [130] zone axis may

be composed of the translational disorder in the *b*-axis direction and the incommensurability in the *a*-axis direction.

The XRD patterns of the surfaces of TiS_2 and $(SnS)_{1.2}(TiS_2)_2$ sintered pellets perpendicular to the pressure direction are shown in **Fig.** 3. Sharp (0 0 *l*) peaks which correspond to the crystal planes perpendicular to the *c*-axis can be observed. Rocking curve is also measured to characterize the degree of orientation. It shows that the full width at half maximum (FWHM) of the (0 0 1) peak of TiS_2 and the (0 0 6) peak of $(SnS)_{1.2}(TiS_2)_2$ are 8.72^o and 8.64^o respectively, showing that the (0 0 *l*) planes are highly oriented and the degree of orientation in TiS_2 and $(SnS)_{1.2}(TiS_2)_2$ is close. The atomic bondings in these two materials are highly anisotropic, and the atomic bonding within the layers must be strong due to high covalency and the interlayer bonding formed mainly by van der Waals force is very weak. Under the pressure during SPS sintering, the crystals tend to slide along the layers and deflect until the layers become aligned perpendicular to the pressure, thereby resulting in high preferred-orientation of the (0 0 *l*) planes. This highly preferred orientation was then supported by two facts. One is that in the direction perpendicular to the pressure, only those zone axis views normal to the *c* axis were observed by TEM, such as [100], [130], and [-350]. The other one is that the electron mobility of the polycrystalline TiS_2 sample with highly preferred orientation is almost comparable to that of single crystals with the same composition. Therefore, it allows an approximate definition of the direction perpendicular to pressure as "in-plane" and the one parallel with it as "cross-plane".

3.2 Thermal stability

TiS_2 has a low thermal stability in air due to oxidation. The TG curve shows that TiS_2 begins to lose its weight at around 533K. In contrast, this oxidation temperature is elevated to 773K for $(SnS)_{1.2}(TiS_2)_2$, showing an improvement of thermal stability (**Fig.** 4). The maximum temperature of the thermoelectric properties measurements for TiS_2 and $(SnS)_{1.2}(TiS_2)_2$ only went to their respective stability limits in air.

3.3 Thermoelectric properties

Both TiS_2 and $(SnS)_{1.2}(TiS_2)_2$ show a metallic electrical conductivity as shown in **Fig.** 5. They also show anisotropic behavior and the "in-plane" values are much higher than the "cross-plane" values. The anisotropy of TiS_2 and $(SnS)_{1.2}(TiS_2)_2$ is much lower than their respective single crystals, because the (0 0 *l*) planes of the polycrystalline samples are not perfectly oriented and any deflection can decrease this anisotropy. However, the degrees of orientation of the (0 0 *l*) planes in TiS_2 and $(SnS)_{1.2}(TiS_2)_2$ are almost the same according to the rocking curve measurement, thereby enabling reasonable comparison of transport properties in the same direction for the two compositions. In the "in-plane" direction, $(SnS)_{1.2}(TiS_2)_2$ has a little higher electrical conductivity than TiS_2 but in the "cross-plane" direction, it has a lower value.

The hall measurement is then performed to analyze the electron transport. It can be shown in **Fig.** 6 that $(SnS)_{1.2}(TiS_2)_2$ has a higher carrier concentration than that of TiS_2. A general viewpoint has been accepted that there exists electron transfer from the MX layer to the TX_2 layers in the misfit layer compounds $(MX)_{1+x}(TX_2)_n$, which also accounts for its stability. [14] In this case, there must be electron transfer from the SnS layer to the TiS_2 layer, resulting in an increase of carrier concentration. The carrier concentration of TiS_2 is higher than that of stoichiometric single crystal TiS_2 [13], due to excess Ti atom into the van der Waals gap, which can hardly be avoided in the synthesis process of TiS_2.

The mobilities for both TiS_2 and $(SnS)_{1.2}(TiS_2)_2$ have a temperature dependency proportional to $T^{-1.5}$, showing that the electrons are mainly scattered by acoustic phonons (**Fig.** 7). The mobilities of the two compositions also show anisotropic behaviors because of the anisotropic structure. It can be noticed that in the in-plane direction, TiS_2 has a mobility of 6.8 $cm^2V^{-1}S^{-2}$ at around 295K, which is rather close to the corresponding value of 7.7 $cm^2V^{-1}S^{-2}$ found in TiS_2 single crystal with the same carrier concentration. [23] This demonstrates that the (0 0 *l*) planes of the polycrystalline samples here are highly oriented so that the in-plane

electron transport properties are close to those of single crystals. In the in-plane direction, the electron mobility of TiS_2 is almost maintained after the intercalation of SnS layers. However, in the cross-plane direction, the SnS layers scatter the transport electrons, resulting in a decrease of mobility.

The Seebeck coefficients of $(SnS)_{1.2}(TiS_2)_2$ are decreased compared with those of TiS_2 in both in-plane and cross-plane directions (**Fig.** 8). It has generally been accepted that 1T-TiS_2 is a semiconductor with an indirect gap of 0.2-0.3 eV, with its conduction and valence bands consisting of Ti 3*d* and S 3*p* states respectively. [24,25] In stoichiometric TiS_2, the Fermi level lies in the bottom of Ti 3*d* band, making multi-valley structure with six small electron pockets around the L-point in the hexagonal Brillouin zone. [13] A high Seebeck coefficient was observed due to large density of states just above the Fermi level as well as phonon-mediated inter-valley. In the nonstiochiometric TiS_2 here, excess Ti atoms reside in the van der Waals gap and become electron donors, resulting in shift of Fermi level into the 3*d* band from the bottom and a decrease of seebeck coefficient. In $(SnS)_{1.2}(TiS_2)_2$, a rigid band model can hold and the band structure is a superposition of those of SnS and TiS_2 subsystem, as in the case of $(SnS)_{1.2}TiS_2$. [18,26,27] The bands near the Fermi level are mainly composed of Ti 3*d*, S 3*p* orbitals of the SnS and TiS_2 subsystems, and Sn 5*s* states. [18] Meanwhile, the position of the Fermi level in the 3*d* orbital of Ti atom can be shifted upward due to bandfilling by those electrons transferred from the SnS layer, Therefore, the Seebeck coefficient was decreased as the density of states decreased. Both TiS_2 and $(SnS)_{1.2}(TiS_2)_2$ show anisotropic Seebeck coefficients, and the Seebeck coefficients in the the in-plane direction are higher than the cross-plane ones. This anisotropy may arise from the anisotropic band structure. In $(SnS)_{1.2}TiS_2$, the bands near the Fermi level show a strong dispersion (about 1 eV) for the directions with a *k* component perpendicular to *c** caused by strong covalent intrerlayer interaction. [18] In the direction parallel with *c**, only several bands (Ti 3d and Sn 5s) with dispersion of about 0.005–0.05 eV is observed. [18]

Both TiS_2 and $(SnS)_{1.2}(TiS_2)_2$ show anisotropic power factors and the in-plane values are higher than the cross-plane ones (**Fig.** 9). In the in-plane direction, the power factor of $(SnS)_{1.2}(TiS_2)_2$ is a little lower than that of TiS_2 and the difference is much higher in the cross-plane direction, mainly due to the electron scattering by the SnS layers.

The thermal conductivities of TiS_2 and $(SnS)_{1.2}(TiS_2)_2$ are shown in **Fig.** 10. $(SnS)_{1.2}(TiS_2)_2$ has lower thermal conductivity than TiS_2 in both in-plane and cross-plane directions in the whole temperature range. Since the thermal conductivity comes from two sources: (1) electrons and holes transporting heat (k_e) and (2) phonons travelling through the lattice (k_l), the electronic thermal conductivity (k_e) is directly related to the electrical conductivity through the Wiedemann-Franz law: $k_e=L_0T\sigma$, where the Lorenz number L_0 is 2.44×10^{-8} $W\Omega K^{-1}$. The values of k_e of these $(MS)_{1+x}(TiS_2)_2$ compositions were calculated and plotted in **Fig.** 10. It can be seen the k_e component is almost close in TiS_2 and $(SnS)_{1.2}(TiS_2)_2$ in both in-plane and cross-plane directions. The main reason of the reduction of the thermal conductivity is the reduction of lattice thermal conductivity, which will be analyzed in detail in the next section.

It has been found that in the in-plane direction, the *ZT* value of $(SnS)_{1.2}(TiS_2)_2$ is much improved compared with TiS_2 due to the superlattice structure (**Fig.** 11), in which the electrons can transmit and phonon velocity is softened. In the cross-plane direction, the *ZT* value is almost unchanged due to simultaneous scattering of both electrons and phonons at the heterointerfaces. Since $(SnS)_{1.2}(TiS_2)_2$ have extremely low thermal conductivity and rather high carrier concentration, the reduction in carrier concentration can reduce the electronic thermal conductivity and optimize the power factor simultaneously, and much higher *ZT* value can be expected to be achieved.

4. Discussion

The lattice thermal conductivity was calculated by subtracting k_e from k, which is shown in **Fig.** 12. It can be noticed that the $(SnS)_{1.2}(TiS_2)_2$ has much lower lattice thermal conductivities than TiS_2 in both in-plane and cross-plane directions. Meanwhile, the minimum thermal conductivity can be calculated for this composition from the equation: [8]

$$k_{\min} = \left(\frac{\pi}{6}\right)^{1/3} k_B n^{2/3} \sum_i v_i \left(\frac{T}{\theta}\right)^2 \int_0^{\theta_i/T} \frac{x^3 e^x}{(e^x - 1)^2} dx \quad (1)$$

The sum is taken over the three sound modes including two transverse and one longitudinal modes with the speed of sound v_i. θ_i is the Debye temperature for each polarization Using the measured values of V_L, V_{T1}, V_{T2}, the k_{min} was calcuated and shown in **Fig.** 12. In the cross-plane direction, k_l of $(SnS)_{1.2}(TiS_2)_2$ is even lower than k_{min}, which can hardly be observed in the bulk materials.

To analyze the ultra-low thermal conductivity, the kinetic theory of thermal conductivity was used.

$$k=1/3C_vVl \quad (2)$$

where C_v, V and l represent the heat capacity, phonon mean free path and speed of sound,, respectively. The heat capacity makes limited contribution to the low thermal conductivity, as the heat capacity approaches $3k_B$ per atom at temperatures higher than the Debye temperature, according to the Dulong-Petit law. Therefore, the reduced thermal conductivity mainly arises from reduction of sound velocity or phonon mean free path.

4.1. Sound velocity

The sound velocity is determined by the density and the elastic constants of a solid. As shown in **Fig.** 13, the sound velocity has three polarization modes, including one longitudinal mode and two transverse modes. In the cross-plane direction, the two transverse velocities are equal because of nearly isotropic structure inside the layers and random orientation of the *a*-*b* planes of different grains. In contrast, in the in-plane direction, the two transverse velocities are not equal because of the layered structure. A pulse-echo method was used to measure

these sound velocities with a 30MHZ longitudinal transducer and a 20MHZ transverse transducer. The measured values are listed in Table 1.

In the in-plane direction, the the longitudinal velocity of $(SnS)_{1.2}(TiS_2)_2$ is a little smaller than that of TiS_2, mainly due to the increase of density. However, the two transverse velocities V_{T1} and V_{T2} are much more decreased, which may arise from the weakening of atomic bonding. The transverse wave is composed of shear movements of atoms, and the velocity is determined by the shear modulus:

$$V_T = \sqrt{\frac{G}{\rho}} \tag{3}$$

where G is the shear modulus and ρ is the density. The shear modulus is calculated by the above equation and shown in Table 1. It can be found that both G_1 and G_2 of $(SnS)_{1.2}(TiS_2)_2$ are much decreased compared with those of TiS_2 because of the intercalated SnS layers. Moreover, G_1 is much lower than G_2 as G_1 is determined by the interlayer bonding while G_2 is determined by the intralayer bonding. The weakened interlayer bonding between the SnS layer and the TiS_2 layer originates from either electrostatic interaction due to electron transfer between these two layers or weak covalent force between the Sn atom and sulfur atoms in the TiS_2 layer. [18,28] The weakened G_2 may be because of the incommensurate structure or disruption of periodicity of the TiS_2 layers in the direction perpendicular to the layers. In the cross-plane direction, the case is similar except that V_{T1} and V_{T2} are equal and both are determined by the weakened interlayer bonding.

4.2. Phonon mean free path

The phonon mean free path in **Fig.** 14 can provide the information of the intensity of phonon scattering in TiS_2 and $(SnS)_{1.2}(TiS_2)_2$. It can be observed that in the in-plane direction, the phonon mean free path is a little decreased. It shows that the in-plane phonons are a little scattered by the interfaces between the SnS layer and TiS_2 layer, as the phonon mean free path here is already rather small here and most phonons don't have to "meet" these interfaces in

transport. In contrast, in the cross-plane direction, the phonon mean free path is significantly decreased. The value even became not physical, as it is lower than the mean atomic distance. However, it unambiguously demonstrates the presence of unusual phonon transport mechanism that is responsible for the low thermal conductivity in this direction.

On one hand, the extremely low mean free path originates from the modulating structure of periodically alternating SnS layer and paired TiS_2 layers. Interface thermal resistance can arise due to the difference of acoustic impedances of these two materials and only a fraction of phonons can transmit across the interfaces. [29,30] However, it is still insufficient to explain the low thermal conductivity, which is even below the theoretical minimum. In the disordered and layered WSe_2 film, the ultralow thermal conductivity is believed to arise from localization of phonons at the interface of two neighboring WSe_2 layers with random orientations. [9] As evidence, ion bombardment (with associated disruption of the crystalline structure inside the layers) can even increase the thermal conductivity. [9] In the "microstructure" section, we have already shown that translational disorder is present in $(SnS)_{1.2}(TiS_2)_2$, which may also induce phonon localization, because the interface of the disorder area is atomically sharp here. In order to test this idea, we substituted Sn with Bi in $((Bi_{0.8}Sn_{0.2})S)_{1.2}(TiS_2)_2$ and the thermal conductivity can even increase above the minimum thermal conductivity (**Fig.** 12). We believe that this substitution can destroy the integer translational shift of SnS layer by random local lattice distortion around those separated point defects, resulting in decrease of the localization of phonons.

The phonon localization behavior can be estimated from the modified Ioffe-regel criteria for Anderson localization. [31,32] It is thought that phonons with $kl \leq 1$ can be considered localized similar to the localization of light in disordered medium, where k and l correspond to wave number and phonon mean free path respectively. [32] The phonon mean free path of $(SnS)_{1.2}(TiS_2)_2$ in the cross-plane direction is in the range of 3.6~3.0 Å from room temperature to 673K, giving rise to cut-off phonon wavelengths of 22.3 Å to 18.6 Å, above

which the phonons are considered to be localized as the $kl \leq 1$ criteria is met. Since the length of the basic unit of $(SnS)_{1.2}(TiS_2)_2$ is 17.4 Å in the same direction, there must be a large portion of localized phonons in the whole phonon spectrum.

In short, the lattice thermal conductivities of $(SnS)_{1.2}(TiS_2)_2$ is dramatically reduced compared with those of TiS_2 in both in-plane and cross-plane directions. In the in-plane direction, the thermal conductivity reduction mainly comes from the softening of the transverse wave with its polarization vertical to the layers. In the cross-plane direction, reduction of thermal conductivity originates from both softening of transverse velocity and enhanced phonon scattering by modulated structure and translational disorder.

5. Conclusions

A natural superlattice with a composition of $(SnS)_{1.2}(TiS_2)_2$ has been "built" by intercalating an SnS layer into the van der Waals gap of layered TiS_2. The HRTEM observation directly demonstrates the superlattice structure, in which one SnS layer and paired TiS_2 layers alternatively stack. By the simulation of the HRTEM pattern, the real crystal structure of $(SnS)_{1.2}(TiS_2)_2$ is reconstructed and the SnS layers show random translational displacements in the direction parallel with the layers. In the direction parallel with the layers, the thermoelectric performance is found to be improved, as the electron mobility is maintained while the phonon transport was suppressed, which is identified due to softening of the transverse waves because of the weakened interlayer bonding. In the direction perpendicular with the layers, the thermal conductivity of $(SnS)_{1.2}(TiS_2)_2$ is even lower than the predicted minimum thermal conductivity and the phonon localization due to the translational disorder of the SnS layers in the direction parallel to the layers possibly accounts for it.

$(SnS)_{1.2}(TiS_2)_2$ shows a relative high *ZT* value and can be considered as promising medium-temperature n-type thermoelectric materials, as it is composed of non-toxic, non-

hazardous and naturally abundant elements. Higher ZT values can be expected, as the carrier concentration has not yet been optimized. Moreover, by varying the species of the host material, the intercalated material as well as the ratio of these two components, we propose a large family of misfit layer compounds $(MX)_{1+x}(TX_2)_n$ (M = Pb, Bi, Sn, Sb, Rare earth elements; T = Ti, V, Cr, Nb, Ta, X = S, Se; n = 1, 2, 3) with natural superlattice structure for possible candidates of high-performance thermoelectric materials, including both *n*-type and *p*-type.

References

1. G. J. Snyder, E. S. Toberer, Nat. Mater. **7**, 105-114 (2008).

2. V. Keppens, D. Mandrus, B. C. Sales, B. C. Chakoumakos, P. Dai, R. Coldea, M. B. Maple, D. A. Gajewski, E. J. Freeman, S. Bennington, Nature **395**, 876-878 (1998).

3. B. C. Sales, D. Mandrus, R. K. Williams, Science **272**, 1325-1328 (1996).

4. K. F. Hsu, S. Loo, F. Guo, W. Chen, J. S. Dyck, C. Uher, T. Hogan, E. K. Polychroniadis, M. G. Kanatzidis, Science **303**, 818-821 (2004).

5. B. Poudel, Q. Hao, Y. Ma, Y. C. Lan, A. Minnich, B. Yu, X. Yan, D. Z. Wang, A. Muto, D. Vashaee, X. Y. Chen, J. M. Liu, M. S. Dresselhaus, G. Chen, Z. Ren, Science **320**, 634-638 (2008).

6. A. I. Hochbaum, R. K. Chen, R. D. Delgado, W. J. Liang, E. C. Garnett, M. Najarian, A. Majumdar, P. D. Yang, Nature **451**, 163-165 (2008).

7. J. S. Rhyee, K. H. Lee, S. M. Lee, E. Cho, S. Il Kim, E. Lee, Y. S. Kwon, J. H. Shim, G. Kotliar, Nature **459**, 965-968 (2009).

8. D. G. Cahill, S. K. Watson, R. O. Pohl, Phys. Rev. B **46**, 6131-6140 (1992).

9. C. Chiritescu, D. G. Cahill, N. Nguyen, D. Johnson, A. Bodapati, P. Keblinski, P. Zschack, Science **315**, 351-353 (2007).

10. R. Venkatasubramanian, E. Siivola, T. Colpitts, B. O'Quinn, Nature **413**, 597-602 (2001).

11. F. J. DiSalvo, Science **285**, 703-706 (1999).

12. Y. K. Koh, C. J. Vineis, S. D. Calawa, M. P. Walsh, D. G. Cahill, Appl. Phys. Lett. **94**, 153101 (2009).

13. H. Imai, Y. Shimakawa, Y. Kubo, Phys. Rev. B **64**, 241104 (2001).

14. G. A. Wiegers, Prog. Solid State Chem. **24**, 1-139 (1996).

15. C. Heideman, N. Nyugen, J. Hanni, Q. Lin, S. Duncombe, D. C. Johnson, P. Zschack, J. Solid State Chem. **181**, 1701-1706 (2008).

16. C. Chiritescu, D. G. Cahill, C. Heideman, Q. Y. Lin, C. Mortensen, N. T. Nguyen, D. Johnson, R. Rostek, H. Bottner, J. Appl. Phys. **104**, 033533 (2008).

17. Y. Oosawa, Y. Gotoh, M. Onoda, Chem. Lett. 523-524 (1989).

18. C. M. Fang, R. A. deGroot, G. A. Wiegers, C. Haas, J. Phys.-Condens. Mat. **8**, 1663-1676 (1996).

19. G. A. Wiegers, A. Meetsma, J. L. Deboer, S. Vansmaalen, R. J. Haange, J. Phys.-Condens. Mat. **3**, 2603-2612 (1991).

20. C. Auriel, A. Meerschaut, R. Roesky, J. Rouxel, Eur. J. Solid State Inorg. Chem. **29**, 1079-1091 (1992).

21. A. Meerschaut, C. Auriel, J. Rouxel, J. Alloy Compd. **183**, 129-137 (1992).

22. A. Meerschaut, L. Guemas, C. Auriel, J. Rouxel, Eur. J. Solid State Inorg. Chem. **27**, 557-570 (1990).

23. P. C. Klipstein, A. G. Bagnall, W. Y. Liang, E. A. Marseglia, R. H. Friend, J. Phys. C Solid State **14**, 4067-4081 (1981).

24. J. A. Wilson, Phys Status Solidi B **86**, 11-36 (1978).

25. J. J. Barry, H. P. Hughes, P. C. Klipstein, R. H. Friend, J. Phys. C Solid State **16**, 393-402 (1983).

26. A. Meerschaut, Curr. Opin. Solid State Mater. Sci. **1**, 250-259 (1996).

27. H. Martinez, C. Auriel, D. Gonbeau, G. Pfister-Guillouzo, A. Meerschaut, J. Electron. Spectrosc. Relat. Phenom. **95**, 145-158 (1998).

28. Y. Ohno, Phys. Rev. B **44**, 1281-1291 (1991).

29. Y. K. Koh, Y. Cao, D. G. Cahill, D. Jena, Adv. Funct. Mater. **19**, 610-615 (2009).

30. E. T. Swartz, R. O. Pohl, Rev. Mod. Phys. **61**, 605-668 (1989).

31. R. Venkatasubramanian, Phys. Rev. B **61**, 3091-3097 (2000).

32. D. S. Wiersma, P. Bartolini, A. Lagendijk, R. Righini, Nature **390**, 671-673 (1997).

Figure captions

Figure 1. HRTEM image of $(SnS)_{1.2}(TiS_2)_2$ along the [100] zone axis. The simulation image using the structure model of $(SnS)_{1.2}TiS_2$ is also present inside the white frame. The right side is the real crystal structure of $(SnS)_{1.2}(TiS_2)_2$, which was reconstructed from the indicated area of the HRTEM image. The dotted line represents the possible interaction between the Sn atoms and the S atoms in the TiS_2 layers.

Figure 2. HRTEM image of $(SnS)_{1.2}(TiS_2)_2$ along the [130] zone axis.

Figure 3. XRD patterns of the surfaces of TiS_2 and $(SnS)_{1.2}(TiS_2)_2$ samples perpendicular to the sintering pressure.

Figure 4. TG curve of TiS_2 and $(SnS)_{1.2}(TiS_2)_2$ in air.

Figure 5. Electrical conductivities of TiS_2 and $(SnS)_{1.2}(TiS_2)_2$ in both in-plane and cross-plane directions.

Figure 6. Carrier concentrations of TiS_2 and $(SnS)_{1.2}(TiS_2)_2$.

Figure 7. Hall mobilites of TiS_2 and $(SnS)_{1.2}(TiS_2)_2$ in both in-plane and cross-plane directions.

Figure 8. Seebeck coefficients of TiS_2 and $(SnS)_{1.2}(TiS_2)_2$ in both in-plane and cross-plane directions.

Figure 9. Power factors of TiS_2 and $(SnS)_{1.2}(TiS_2)_2$ in both in-plane and cross-plane directions.

Figure 10. Total thermal conductivities (k) and the electron component (k_e) of TiS_2 and $(SnS)_{1.2}(TiS_2)_2$ in both in-plane and cross-plane directions.

Figure 11. ZT values of TiS_2 and $(SnS)_{1.2}(TiS_2)_2$ in both in-plane and cross-plane directions.

Figure 12. Lattice thermal conductivities of TiS_2 and $(SnS)_{1.2}(TiS_2)_2$ in both in-plane and cross-plane directions. The calculated minimum thermal conductivities (k_{min}) of $(SnS)_{1.2}(TiS_2)_2$ are included. The lattice thermal conductivity of $(Sn_{0.8}Bi_{0.2}S)_{1.2}(TiS_2)_2$ in the cross-plane direction is also plotted.

Figure 13. Schematic illustration of the longitudinal and transverse sound velocities in layered TiS_2 and $(SnS)_{1.2}(TiS_2)_2$ in both in-plane and cross-plane directions.

Figure 14. Phonon mean free paths of TiS_2 and $(SnS)_{1.2}(TiS_2)_2$ in both in-plane and cross-plane directions.

Figure 1

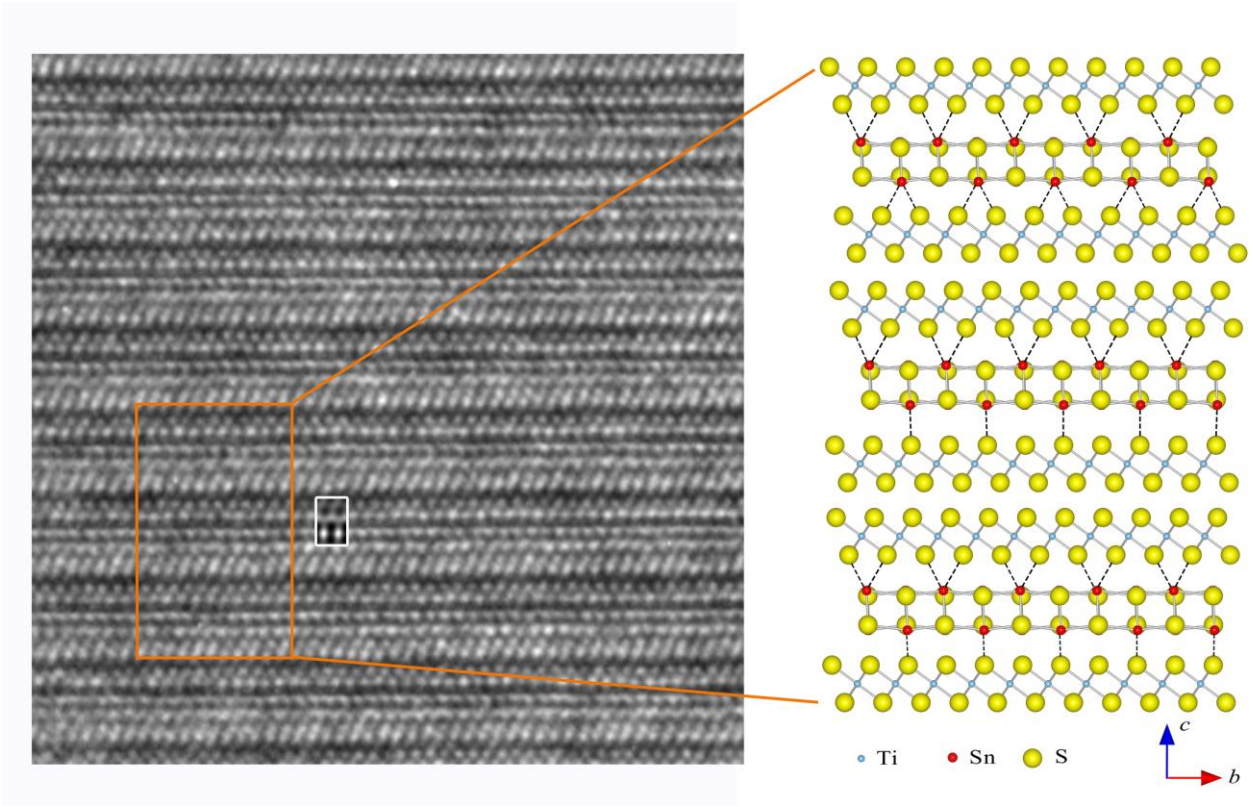

Figure 2

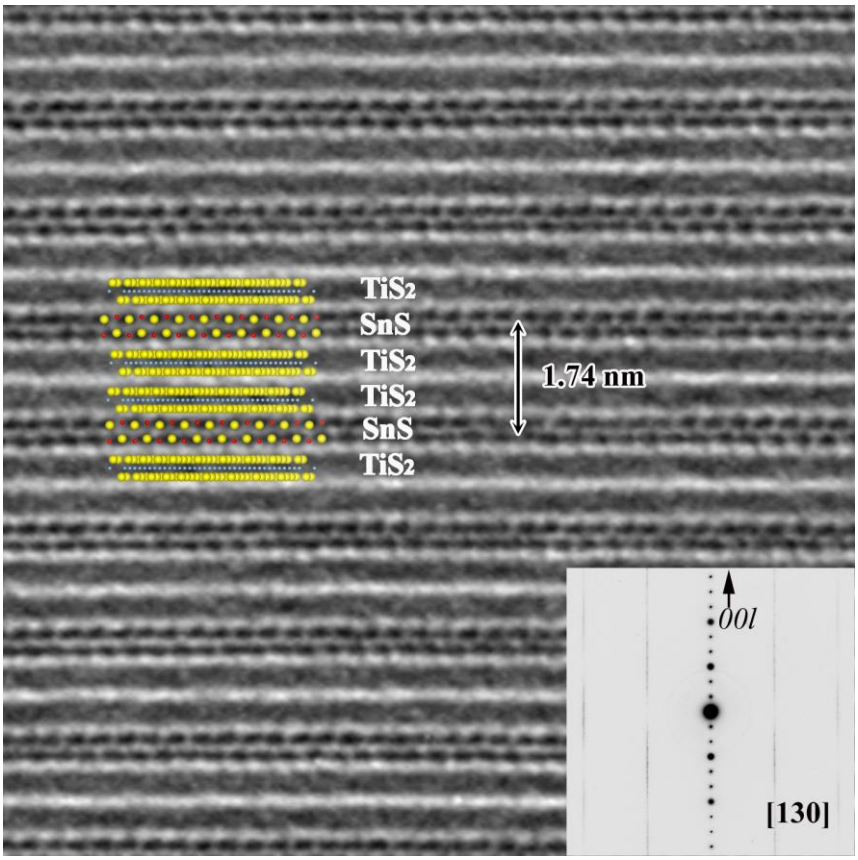

Figure 3

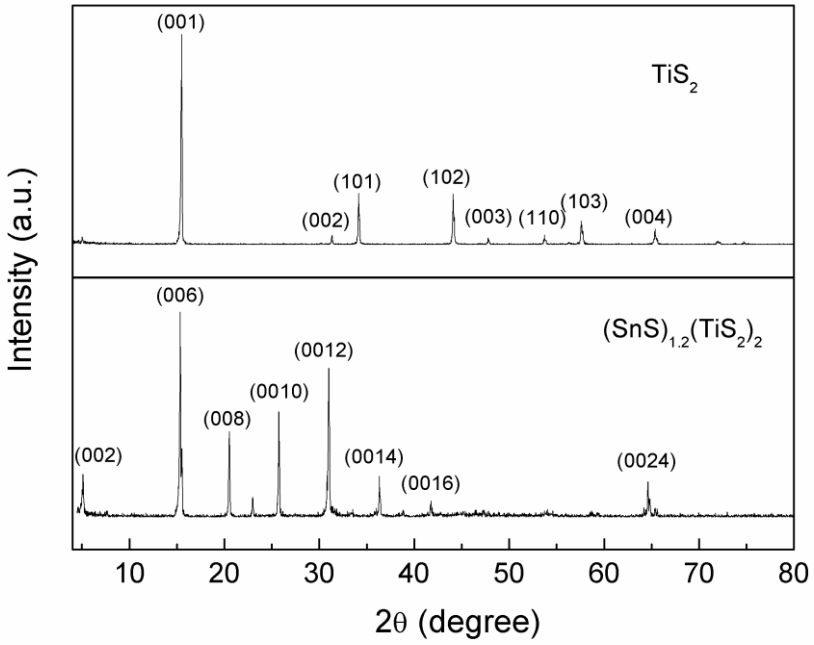

Figure 4

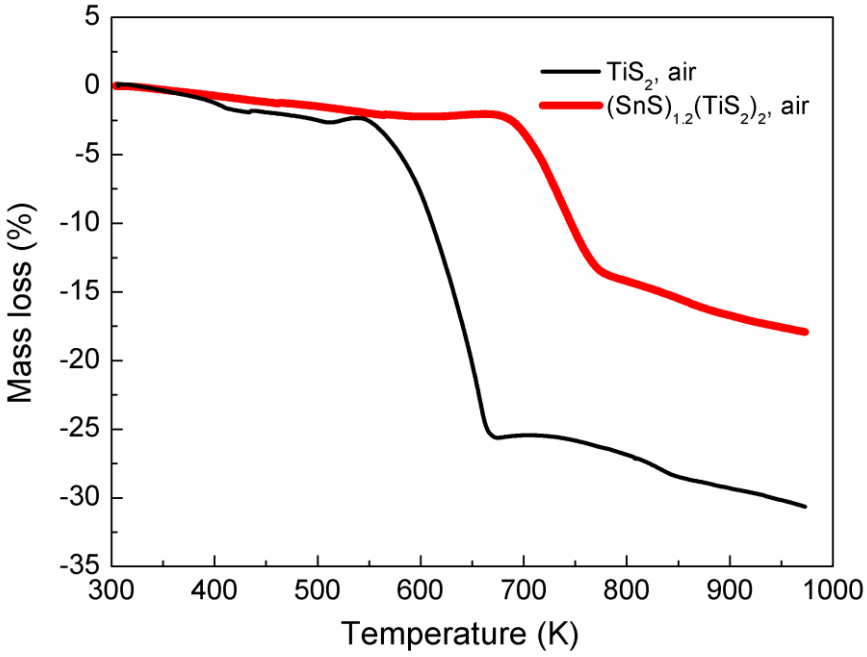

Figure 5

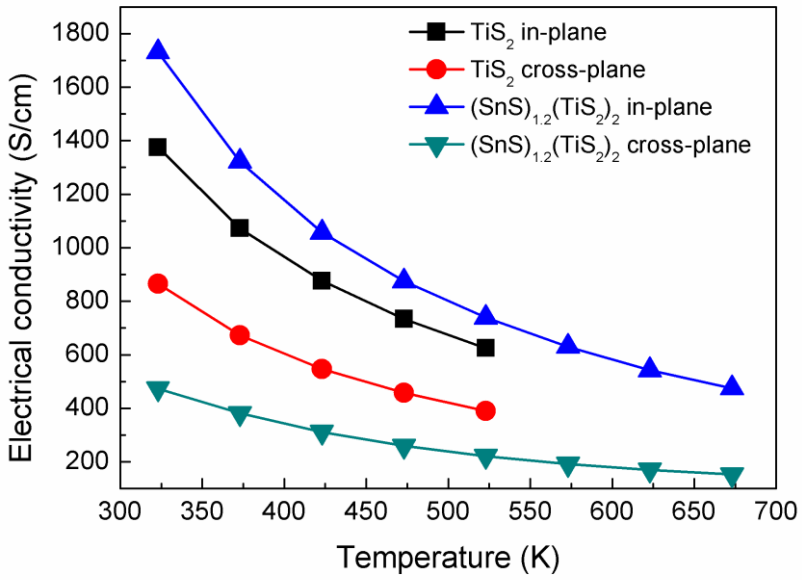

Figure 6

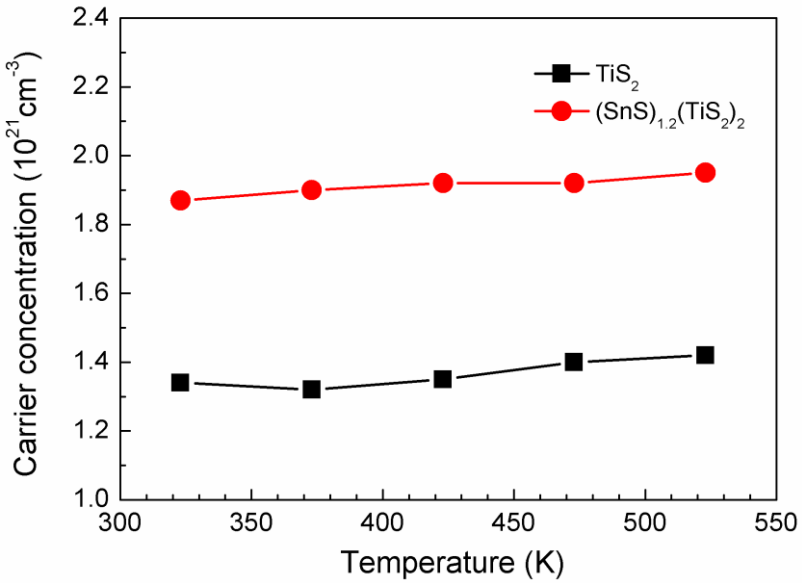

Figure 7

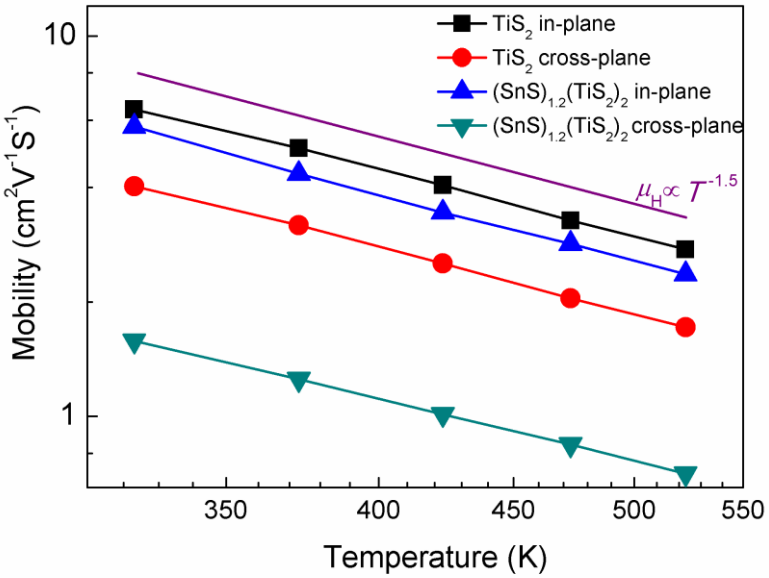

Figure 8

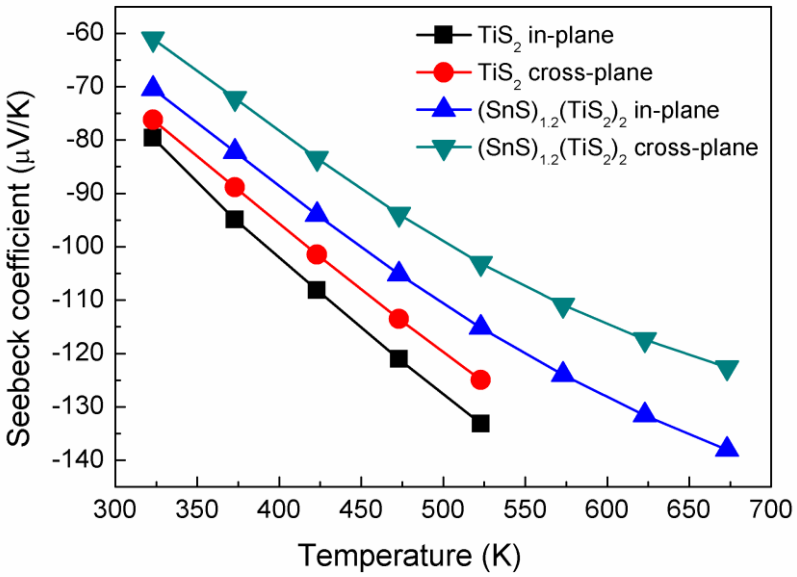

Figure 9

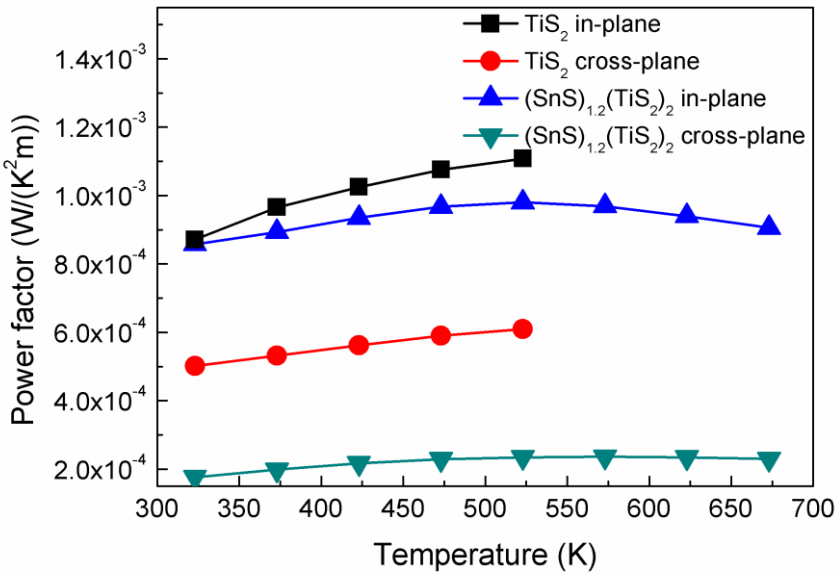

Figure 10

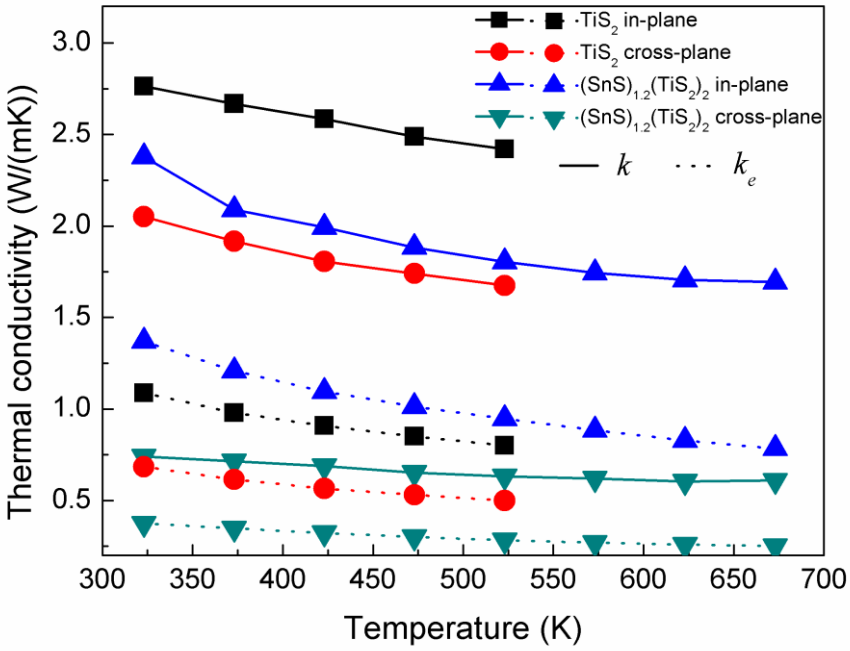

Figure 11

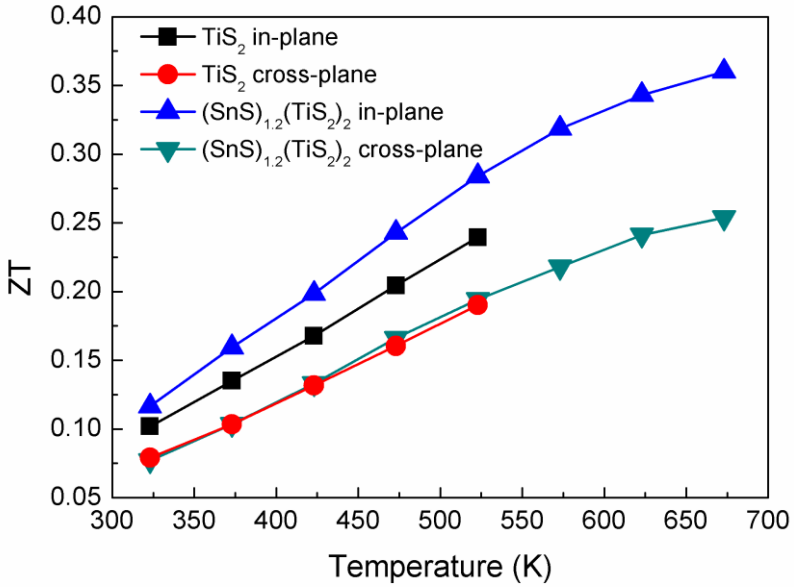

Figure 12

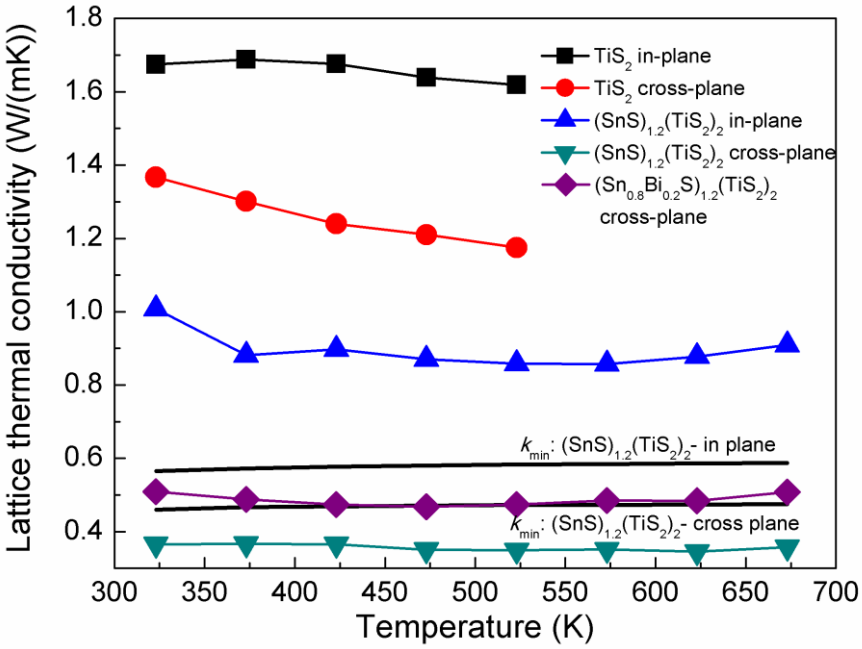

Figure 13

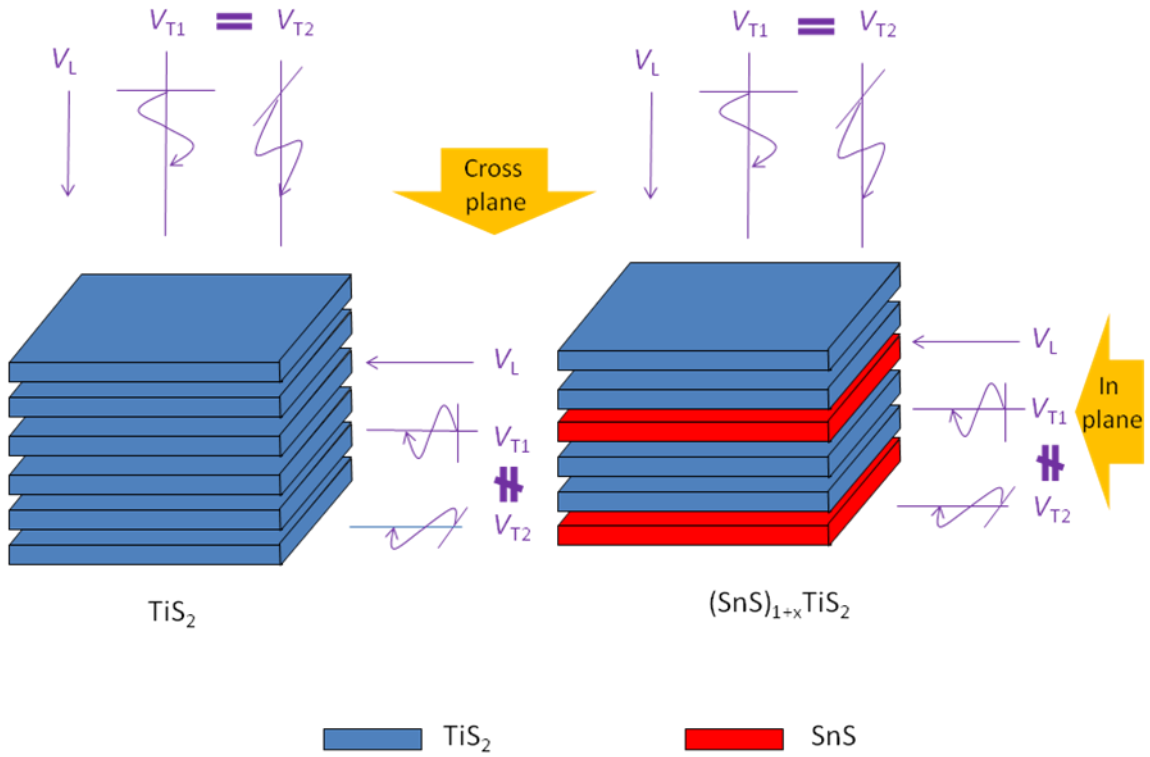

Figure 14

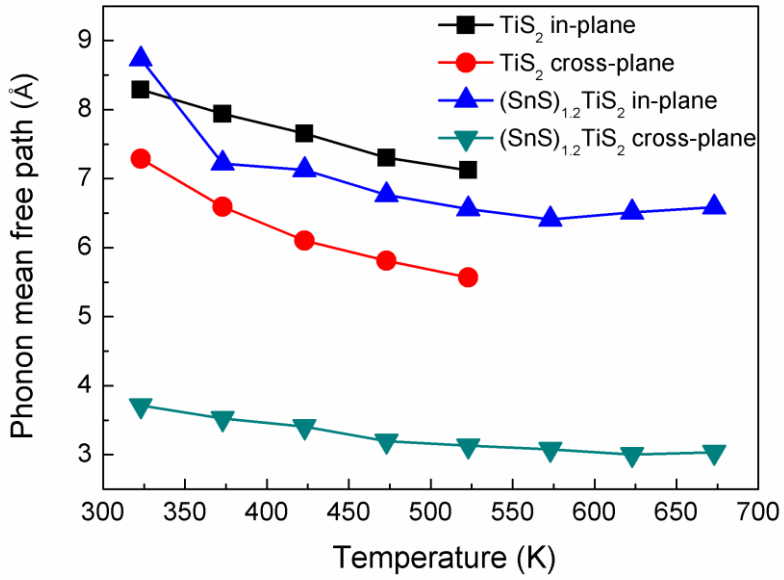

Table 1. Densities, longitudinal and transverse sound velocities, and corresponding shear moduli of TiS_2, and $(SnS)_{1.2}(TiS_2)_2$ in both of the in-plane and cross-plane directions.

Material	Direction	ρ [g/cm^3]	V_L [m/s]	V_{T1} [m/s]	V_{T2} [m/s]	G_1 [Gpa]	G_2 [Gpa]
TiS_2	In-plane	3.21	5284	2799	3295	25.0	34.7
	Cross-plane		4383	2825		25.6	
$(SnS)_{1.2}(TiS_2)_2$	In-plane	3.87	4111	1578	2352	9.6	21.4
	Cross-plane		3368	1555		9.4	